

SCIENTIFIC REPORTS



OPEN

Temperature-Controlled Direct Imprinting of Ag Ionic Ink: Flexible Metal Grid Transparent Conductors with Enhanced Electromechanical Durability

Yong Suk Oh¹, Hyesun Choi¹, Jaeho Lee², Hyunwoo Lee², Dong Yun Choi³, Sung-Uk Lee¹, Kyeong-Soo Yun¹, Seunghyup Yoo², Taek-Soo Kim¹, Inkyu Park¹ & Hyung Jin Sung¹

Next-generation transparent conductors (TCs) require excellent electromechanical durability under mechanical deformations as well as high electrical conductivity and transparency. Here we introduce a method for the fabrication of highly conductive, low-porosity, flexible metal grid TCs *via* temperature-controlled direct imprinting (TCDI) of Ag ionic ink. The TCDI technique based on two-step heating is capable of not only stably capturing the Ag ionic ink, but also reducing the porosity of thermally decomposed Ag nanoparticle structures by eliminating large amounts of organic complexes. The porosity reduction of metal grid TCs on a glass substrate leads to a significant decrease of the sheet resistance from 21.5 to 5.5 $\Omega \text{ sq}^{-1}$ with an optical transmittance of 91% at $\lambda = 550 \text{ nm}$. The low-porosity metal grid TCs are effectively embedded to uniform, thin and transparent polymer films with negligible resistance changes from the glass substrate having strong interfacial fracture energy ($\sim 8.2 \text{ J m}^{-2}$). Finally, as the porosity decreases, the flexible metal grid TCs show a significantly enhanced electromechanical durability under bending stresses. Organic light-emitting diodes based on the flexible metal grid TCs as anode electrodes are demonstrated.

Transparent conductors (TCs) are indispensable in a variety of optoelectronic devices, including organic light-emitting diodes (OLEDs), organic solar cells, and touch screen panels¹. Indium tin oxide (ITO)-based films have been the industrial standard for a long time due to their low electrical sheet resistance (R_s) and high optical transmittance (T); however, ITO-based films include several drawbacks, including inherent brittleness and the need for expensive sputtering processes². Alternative materials to ITO-based films, including conducting polymers³, graphene⁴, carbon nanotubes⁵, random metal nanowire networks^{6–10}, and regular metal grids¹¹, have been reported for use in flexible optoelectronic devices. Among these materials, regular metal grids offer many advantages, such as facile control over their grid width and spacing, scalability to large-area application and low junction resistance^{12,13}.

Cost-effective and solution-processed metal grid TCs on flexible substrates have been reported using two different fabrication schemes: (1) grid-patterned cavity is formed into a polymer substrate using hot embossing process and then is filled with metal nanoparticle (NP) ink^{14–16}. This method facilitates the fabrication of metal grid structures with the relatively high aspect ratio (=height/width), while they should be sintered at low temperature ($< 150^\circ\text{C}$) due to thermal degradation of the polymer substrate; (2) metal NP structures on a glass substrate are fabricated using a variety of wet deposition methods, such as direct imprinting (DI)^{17,18}, gravure printing¹⁹, electrohydrodynamic jet printing^{20,21} and inkjet printing²². Although this method is not suitable for fabricating the high aspect ratio structures of metal NPs, the metal grid TCs on the glass substrate can be sintered

¹Department of Mechanical Engineering, Korea Advanced Institute of Science and Technology, Daejeon, 34141, Korea. ²Department of Electrical Engineering, Korea Advanced Institute of Science and Technology, Daejeon, 34141, Korea. ³Powder & Ceramics Division, Korea Institute of Materials and Science, Changwon, 51508, Korea. Correspondence and requests for materials should be addressed to I.P. (email: inkyu@kaist.ac.kr) or H.J.S. (email: hjsung@kaist.ac.kr)

at high-temperatures ($>200^{\circ}\text{C}$) to improve the electrical conductivity^{23,24}. After high-temperature sintering process, the metal grid TCs are transferred from the glass substrate to the polymer substrate for the fabrication of flexible metal grid TCs.

Among the wet deposition methods, the DI of colloidal metal NPs can directly produce micro/nanoscale metal structures at low-costs and in a high-throughput manner without expensive etching steps and metal evaporation^{25,26}. Recently, our group suggested a reservoir-assisted DI method based on an Ag ionic ink, which has several advantages such as higher metal content and less aggregation than colloidal metal NPs, for the fabrication of high-performance flexible metal grid TCs^{17,18}. However, the Ag NP structures fabricated by the thermal decomposition of Ag ionic ink include numerous micro/nanoscale pores due to the elimination of organic complexes^{27,28}. Unfortunately, those pores can deteriorate electrical and mechanical properties of the flexible metal NP structures^{29–33}. First, the formation of many pores precludes the generation of highly conductive metal grid TCs. Second, since high-temperature sintering process ($\sim 300^{\circ}\text{C}$) induces strong interfacial fracture energy (IFE) between the metal and the substrate, micro/nanoscale pores can cause serious damage to metal NP structures during the transfer process. Finally, as the cracks are initiated and propagated near numerous pores under mechanical deformations, the flexible metal grid TCs may be easily damaged by static or dynamic bending stresses. The formation of micro/nanoscale pores inside the metal NP structures should be minimized in the development of flexible optoelectronic applications.

In order to resolve this problem, we introduce a novel temperature-controlled direct imprinting (TCDI) process of Ag ionic ink based on two-step heating for the generation of highly conductive, low-porosity, flexible metal grid TCs. This TCDI technique led to stably capturing the Ag ionic ink and reducing the porosity of thermally decomposed Ag NP structures. The electrical resistivity (ρ_m) and R_s of the metal grid TCs at a fixed transmittance ($T_{550\text{nm}}$) at 550 nm were represented as a function of the organic complex contents and geometrical calculation. The effect of porosity on the transfer process of metal grid TCs to the polymer film was explored at different sintering temperatures. In addition, the effect of porosity on an electromechanical durability of the flexible metal grid TCs was examined under the static and dynamic bending stresses. Finally, the utility of flexible metal grid TCs as anode electrodes was demonstrated by fabricating of OLEDs.

Results

Temperature-controlled direct imprinting of Ag ionic ink. The TCDI of Ag ionic ink, which involves the two-step heating, is schematically illustrated in Fig. 1a: (i) Ag ionic ink ($10\ \mu\text{L}$) was imprinted on a fluorinated glass substrate using a grid-patterned mold under low pressure ($P = 120\ \text{kPa}$) and low temperature; (ii) the first heating step was performed at an evaporation temperature (T_E) of 50°C over 5 min to stably capture the Ag ionic ink inside the grid-patterned cavity. It should be noted that when the Ag ionic ink is initially heated at an increased T_E , large amounts of the filled ink leave from the grid-patterned cavity through a liquid film between the mold and the substrate due to carbon dioxide generation during the thermal decomposition of Ag ions³⁴; (iii) for a liquid film with negligible thickness ($h_f \approx 0$), the second heating step was carried out at decomposition temperature (T_D) = 90°C to eliminate organic complexes derived from the thermal decomposition of the Ag ions and to improve their thermal decomposition rate; (iv) after complete solvent evaporation, the grid-patterned mold was carefully removed from the substrate. The Ag NP structures were thermally treated at sintering temperature (T_S) = 300°C for 10 min. Figure 1b shows a schematic illustration of (i) the two-step heating of TCDI and (ii) the one-step heating of typical DI, respectively. In Fig. 1b(iii–iv), focused ion beam-scanning electron microscope (FIB-SEM) images show a cross-section of the metal grid line structures fabricated using TCDI and DI of Ag ionic ink, respectively. As T_D was increased from 50°C to 90°C , the micro/nanoscale pores in the metal grids were significantly reduced. This micro/nanoscale pores may be mainly generated by the elimination of organic complexes during the thermal decomposition process. Amounts of organic complexes inside the Ag NP structures were compared using thermogravimetric analysis (TGA) and derivative thermogravimetric (DTG) analysis of Ag NP-organic complex powders, respectively. Figure 1c shows the TGA and DTG curves obtained from Ag NP-organic complex powders after complete drying at $T_D = 50$ and 90°C , respectively. The Ag NP-organic complex powders dried at the lower T_D showed the larger weight loss and the faster decomposition rate in the temperature range of 100 – 200°C . The Ag NP-organic complex powders dried at $T_D = 50$ and 90°C showed a weight loss of 21.24 and 6.17%, respectively. These results indicated that the metal grids generated using the DI of Ag ionic ink may include a greater fraction of the organic complex by weight, about 15% more, than those obtained using the TCDI of Ag ionic ink. Figure 1d plots a weight loss of the Ag NP-organic complex powders dried at different values of T_D . As T_D increased from 50 to 100°C , the organic complex contents of the powder decreased. The inset shows photographic images of the metal-organic complex powders. The Ag NP-complex powders dried at $T_D = 50^{\circ}\text{C}$ showed dark black due to high organic complex contents (left), while those obtained at $T_D = 90^{\circ}\text{C}$ showed bright silver due to relatively low organic complex contents (right).

Highly conductive, low-porosity metal grid TCs. Figure 2a shows a SEM image of the Ag NP structures fabricated over the grid-patterned mold area ($10.5\ \text{mm} \times 10.5\ \text{mm}$). The presence of unwanted residual layers within the grid spacing was negligible. The inset shows a magnified SEM image of the Ag NP structures at the intersection of metal grids. A linewidth ($\sim 8\ \mu\text{m}$) of the metal grid was smaller than that of the original grid-patterned cavity ($15\ \mu\text{m}$) due to mold deformation. Figure 2b shows the values of R_s and $T_{550\text{nm}}$ for the metal grid TCs generated using the TCDI of Ag ionic ink. As T_D increased from 50 to 90°C , R_s of the metal grid TCs decreased significantly, holding $T_{550\text{nm}}$ over 91.2%; however, the value of R_s for the metal grid TCs fabricated at $T_D = 100^{\circ}\text{C}$ increased and fluctuated as solvent evaporation and thermal decomposition occurred near the boiling point of the base-solvent (toluene, 110.6°C). Figure S1(a) shows transmittance spectra over a wavelength range of 350–800 nm of the metal grid TCs fabricated at different values of T_D . The spectral transmittance of metal grid TCs fabricated at $T_D = 100^{\circ}\text{C}$ did significantly decrease from 350 to 500 nm. Also, figure of merit (FoM),

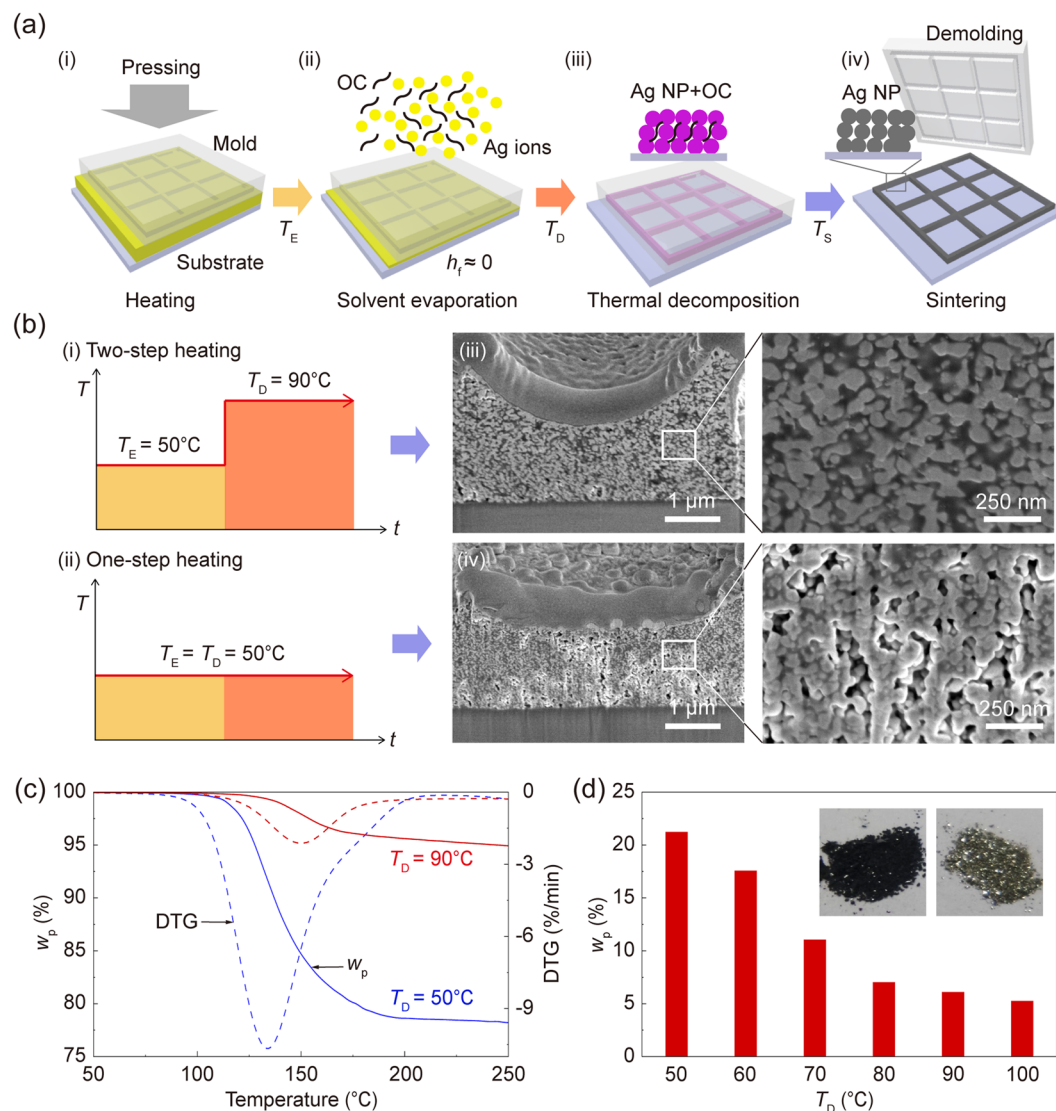


Figure 1. (a) The TCDI of Ag ionic ink. (b) (i-ii) Schematic illustration of the two-step heating of TCDI and the one-step heating of typical DI, respectively. (iii-iv) Cross-sectional FIB-SEM images and magnified SEM images of the metal grid line structures fabricated using TCDI and DI of Ag ionic ink, respectively. (c) TGA and DTG curves obtained from the metal-organic complex powders as a function of T_D . (d) Weight percent of metal-organic complex powders, as a function of T_D . The inset shows photographs of the metal-organic complex powders, dried at two different values of $T_D = 50$ and 90°C for 3 hour, respectively.

which generally predicts the performances of TCs, was compared for the metal grid TCs generated at different values of T_D in Figure S1(b). As T_D increased to 90°C , the FoM of the metal grid TCs was increased from 250 to 572. The value of ρ_m of thermally reduced Ag NP line structures fabricated at different values of T_D is compared in Fig. 2c. The value of ρ_m could be expressed using the following relationship:

$$\rho_m(x) = \rho_0 \exp(k_p w_p), \quad (1)$$

where ρ_0 is the electrical resistivity of the thermally reduced metal structures without organic complex contents, w_p is the weight percent of organic complex and k_p is a correction factor from experimental data. The correction factor was determined to be $k_p = 0.0727$. The value of ρ_0 ($6.5287 \times 10^{-6} \Omega \text{ cm}$) was 4 times larger than that of the bulk Ag ($1.59 \times 10^{-6} \Omega \text{ cm}$).

The R_s of the metal grid TCs was calculated based on the structural size and organic complex weight. The equation used to predict R_s was constructed by modifying the expression for R_s obtained using a square wire network, as suggested by Van de Groep *et al.*¹³. The cross-section of the Ag NP structures was regarded as trapezoidal, and R_s was predicted using the following equation:

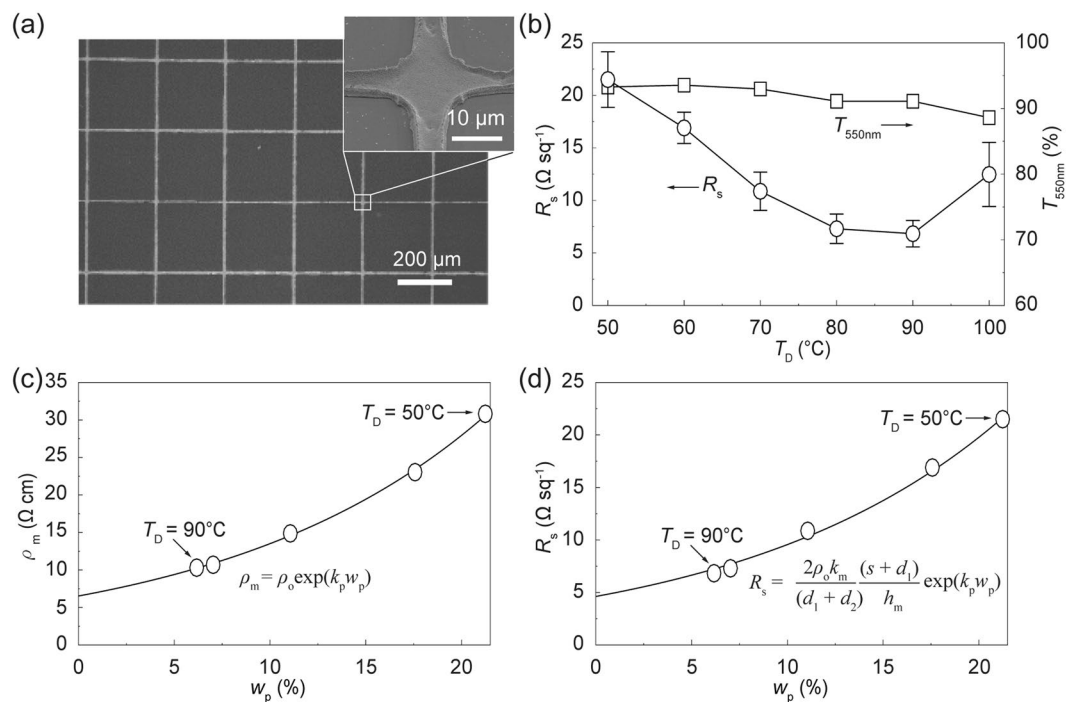


Figure 2. (a) A SEM image of the metal grid TCs fabricated using the TCDI of Ag ionic ink. The inset shows a magnified SEM image of the intersection in the Ag NP structure. (b) Sheet resistance of the metal grid TCs generated at different values of T_D . (c) Electrical resistivity of the Ag NP structures as a function of the organic complex weight. (d) Sheet resistance of the metal grid TCs as a function of the organic complex weight.

$$R_s = \frac{2\rho_m k_m}{(d_1 + d_2)} \frac{(s_m + d_1)}{h_m} = \frac{2\rho_o k_m}{(d_1 + d_2)} \frac{(s_m + d_1)}{h_m} \exp(k_p w_p), \quad (2)$$

where h_m is the thickness of the metal grid line, d_1 is the bottom width and d_2 is the top width of the metal grid line, and s is the spacing between the metal grid lines. The value of k_m depends on a difference between the predicted shape of the Ag NP structures and their actual shape. The mean values of d_1 , d_2 , h_m , s_m for the metal grid line were 8 μm , 6 μm , 2 μm and 257 μm , respectively. The correction factor, extracted from experimental results, was determined to be $k_m = 3.74$. Figure 2d indicates that the R_s of the metal grid TCs fabricated at different values of T_D could be suitably fit to the theoretical values.

Transfer process of metal grid TCs. The metal grid TCs on the glass substrate should be transferred onto the polymer substrate for use in flexible optoelectronic devices. A transfer process of metal grid TCs provided the flexibility and significantly reduced the surface roughness that can cause optoelectronic device failure. Figure 3a shows a schematic illustration of the transfer process, based on a sandwich structure (glass substrate/polymer film/glass substrate) to generate a uniform, thin and transparent polymer film on both sides. It should be noted that when the polymer film becomes thinner, the flexible metal grid TCs show better electromechanical durability under the same bending radius (r) due to a decrease of the nominal bending strain³⁵. The Norland Optical Adhesive 81 (NOA 81), which shows a high optical transparency over a wide spectral range with a good mechanical flexibility and a strong adhesion force to metal structures, is used as the polymer film. The NOA 81 solution was poured onto the metal grids-patterned glass substrate, and then was covered by the glass substrate. After the UV exposure, the metal grids embedded within NOA 81 film were detached from two glass substrates.

The effect of the porosity reduction on the transfer process of metal grid TCs was explored by measuring the resistance changes of metal grid TCs sintered at different values of T_s . The higher T_s induces the more increase of the IFE between the metal and the glass substrate, which causes serious damage to the flexible metal grid TCs during the transfer process. Especially, the metal structures with many pores are prone to be broken due to the increase of the IFE. In Figure S2(a), the IFE of Ag NP film on the glass substrate was quantitatively measured using a double cantilever beam (DCB) fracture mechanics testing method at different values of T_s . In Figure S2(b), the inset shows a schematic diagram of the DCB test specimen consisting of a fluorinated glass substrate (donor substrate), a Ag NP film, an adhesion layer, and the plasma-treated glass substrate (receiving substrate). Figure 3b plots the IFE between the Ag NP film and the substrate after T_s over the range 200–300 $^{\circ}\text{C}$. Although the glass substrate was treated by the fluorine, the IFE between the Ag NP film and the glass substrate depended strongly on T_s . The Ag NP films sintered at $T_s = 300$ $^{\circ}\text{C}$, in particular, displayed 3-fold larger IFE (~ 8.2 J m^{-2}) than those sintered at $T_s = 200$ $^{\circ}\text{C}$ (~ 2.7 J m^{-2}). Figure 3c shows the normalized resistance change ($\Delta R/R_o$) and R_s of the flexible metal grid TCs after the transfer process of the metal grid TCs sintered $T_s = 200$ –300 $^{\circ}\text{C}$. As T_s increased, $\Delta R/R_o$ of the flexible metal grid TCs based on the DI of Ag ionic ink ($T_D = 50$ $^{\circ}\text{C}$) significantly increased from

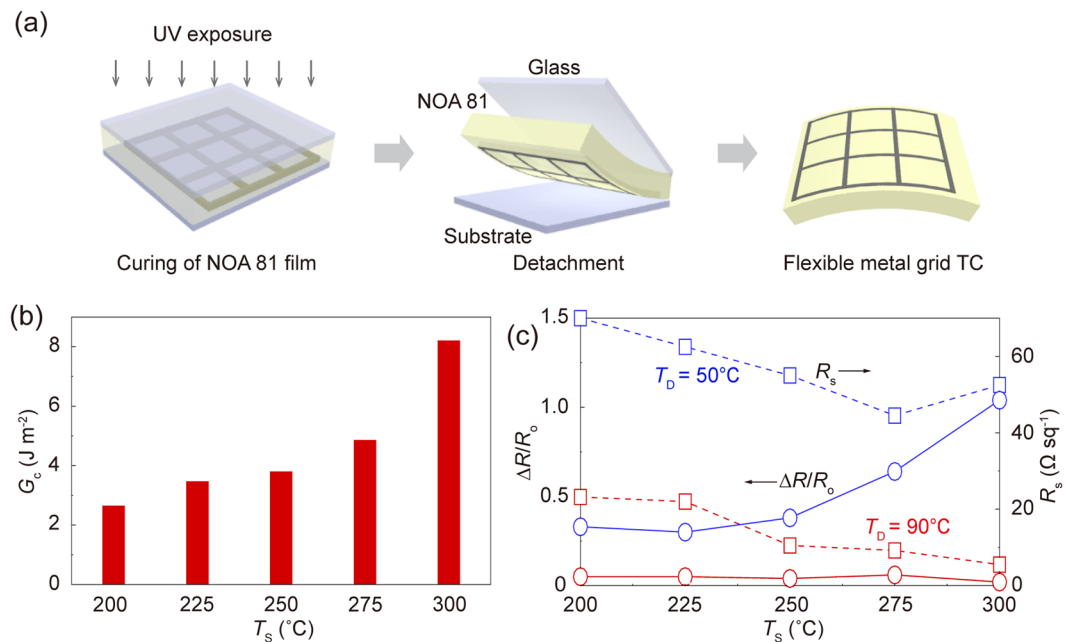


Figure 3. (a) Schematic illustration of the process used to transfer the metal grid TC from the glass substrate to the transparent polymer film (NOA 81 film). (b) Interfacial fracture energy of the Ag NP film sintered at different values of T_s . (c) Normalized resistance changes of the metal grid TCs and the flexible metal grid TCs after the transfer process. The resistance of the flexible metal grid TCs sintered at different T_s for comparison.

33% to ~104% due to an increase of the IFE. On the other hand, the flexible metal grid TCs obtained using the TCDI of Ag ionic ink ($T_D = 90^\circ\text{C}$) displayed a small value of $\Delta R/R_0$ (~6%). Although the IFE increased, the porosity reduction led to preventing a significant increase in $\Delta R/R_0$ from serious mechanical damage. The R_s of the flexible metal grid TCs fabricated at $T_D = 50$ and 90°C showed 5.5 and 52.5 $\Omega\text{ sq}^{-1}$, respectively.

Highly conductive, low-porosity, flexible metal grid TCs. Figure 4a(i) shows a cross-sectional FIB-SEM image of the metal grid-embedded the NOA 81 film. The metal grid structures were buried below the NOA 81 surface. Figure 4a(ii) shows an atomic force microscopy (AFM) surface profile of the flexible metal grid TCs, which presented smooth surfaces with a root-mean-square surface roughness of 6.7 nm and a maximum peak-to-valley value of 43.8 nm. Figure 4b compares the values of T and R_s for the flexible metal grid TCs with the values obtained from a commercially available ITO-coated polyethylene terephthalate (PET) film. Here, it should be noted that the transmittance spectra of the bare NOA 81 film, the flexible metal grid TCs, and the ITO-coated PET film include the transmittance through the substrate. The flexible metal grid TCs performed better (R_s of 5.5 $\Omega\text{ sq}^{-1}$ and $T_{550\text{nm}}$ of 81.47%) than the ITO-coated PET film (R_s of 15.0 $\Omega\text{ sq}^{-1}$ and $T_{550\text{nm}}$ of 78.35%). The T of the ITO-coated PET film fluctuated over the wavelength range of 350–800 nm, whereas the corresponding values of the flexible metal grid TCs remained constant.

The electromechanical durability of the flexible metal grid TCs under static and dynamic bending stresses is an important factor to be considered in flexible optoelectronic devices^{35,36}. As the number of pores in the metal grid structures decreased, the mechanical durability of the flexible metal grid TCs can be improved by inhibiting pore-induced crack initiation and propagation under bending stresses^{29–33}. This resulted in reducing the electrical resistance changes of the metal grid structures under bending stresses. Figure 4c plots the values of $\Delta R/R_0$ obtained from the flexible metal grid TCs fabricated using TCDI and DI of Ag ionic ink under a static bending test. The value of $\Delta R/R_0$ of the ITO-coated PET film under a static bending test was evaluated as a reference. As the flexible metal grid TCs were bent up to $r = 1$ mm, the values of $\Delta R/R_0$ increased for these two flexible metal grid TCs ($R_0 = 6.3$ and 21.0 $\Omega\text{ sq}^{-1}$) by a factor of 2.2 and 113.3 respectively. The R/R_0 of the flexible metal grid TCs fabricated using the DI of Ag ionic ink significantly increased at $r = 1$ mm due to serious damage. Figure 4d plots the values of $\Delta R/R_0$ obtained from the flexible metal grid TCs fabricated using TCDI and DI of Ag ionic ink under a dynamic bending test with $r = 7.5$ mm. The value of $\Delta R/R_0$ of the ITO-coated PET film under a dynamic bending test was evaluated as a reference. After the only several bending cycles, the resistance of the ITO-coated PET film significantly increased to a few tens of k Ω due to formation of numerous and visible cracks. After 1000 cycles of repeated bending/relaxation, $\Delta R/R_0$ obtained from the flexible metal grid TCs ($R_0 = 7.4$ and 43.5 $\Omega\text{ sq}^{-1}$) increased by a factor of 1.5 and 86.4, respectively. When T_D increased, the porosity reduction of the flexible metal grids led to decreasing $\Delta R/R_0$ under static and dynamic bending stresses (a significant decrease in the relative ratio of resistance change by more than 51 times at $r = 1$ mm and by more than 57 times after the 1000 bending cycles, respectively). The low-porosity, flexible metal grid TCs fabricated using the TCDI of Ag ionic ink showed

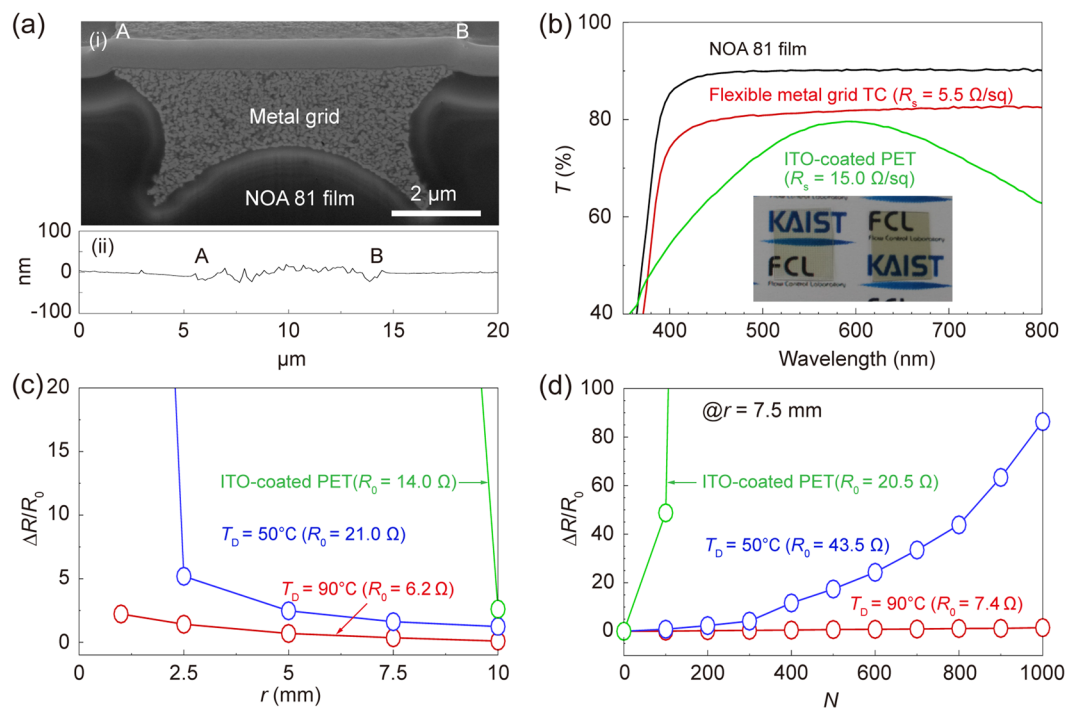


Figure 4. (a-i) A cross-sectional surface of the metal grid TCs-embedded within the NOA 81 film. (a-ii) AFM surface profile of the metal grids TCs within the NOA 81 film. (b) Transmittance spectra over a wavelength range of 350–800 nm, of the NOA 81 film, the metal grid TCs-embedded within the NOA 81 film, and the ITO-coated PET film, respectively. The inset shows photographs of the metal grids TC-embedded NOA 81 film (left) and ITO-coated PET film (right). (c) Normalized resistance changes of the flexible metal grid TCs ($T_D = 50$ and 90°C , respectively) and ITO-coated PET film as a function of the bending radius. (d) Normalized resistance change of flexible metal grid TCs ($T_D = 50$ and 90°C , respectively) and ITO-coated PET film during the dynamic bending tests.

an excellent electromechanical durability under static and dynamic bending tests, indicating their great potential for use in various flexible optoelectronic devices.

Discussion

Applications to flexible organic light-emitting diodes. Figure 5a shows a schematic diagram of OLEDs based on the flexible metal grid TCs. Indium zinc oxide (IZO) layers with a thickness of 50 nm were used to cover the flexible metal grid TCs, which exhibit R_s of $5.5 \Omega \text{sq}^{-1}$ and $T_{550\text{nm}}$ of 81.47%. Poly(3,4-ethylenedioxythiophene) polystyrene sulfonate (PEDOT:PSS) and MoO_3 layers were used on the top of IZO films for efficient hole injection. The 4,4'-Bis(N-carbazolyl)-1,1'-biphenyl (CBP) layer doped with green phosphorescent emitters of bis(2-(2-pyridinyl-N)phenyl-C)(acetylacetonate) iridium (III) ($\text{Ir}(\text{ppy})_2\text{acac}$, 7 wt%) was used as an emitting layer. The CBP and 2,2',2''-(1,3,5-Benzinetriyl)-tris(1-phenyl-1-H-benzimidazole) (TPBi) layers were used as hole- and electron- transport layers, respectively. Figure 5b shows the normalized electro-luminescence spectrum of the flexible OLEDs in the normal direction in the wavelength range of 350–700 nm, which is similar to that of the ITO-based TCs. The inset shows the operating image of the flexible OLEDs under bending. The OLEDs fabricated on the flexible metal grid TCs show an electrically stable operation due to their relatively good uniformity and low roughness, as shown in Fig. 5c. The inset shows the angular emission profile, which was used to obtain the external quantum efficiency (η_{EQE}) and power efficiency (η_{PE}) of the devices. Therefore, the OLEDs based on the flexible metal grid TCs show the comparable values of η_{EQE} and η_{PE} with those of ITO-based OLEDs, as shown in Fig. 5d. The flexible OLEDs exhibit η_{EQE} of 22.0% and η_{PE} of 61.8lm W^{-1} at 111.6cd m^{-2} , while ITO-based OLEDs show η_{EQE} of 21.5% and η_{PE} of 60.6lm W^{-1} at 116.2cd m^{-2} , respectively.

In summary, we demonstrated the fabrication of highly conductive, low-porosity, flexible metal grid TCs via the TCDI of Ag ionic ink. As T_D increased during the thermal decomposition of Ag ionic ink, the porosity of metal grid structures was significantly reduced due to the elimination of large amounts of organic complexes. Also, both ρ_m and R_s of metal grid TCs were estimated based on the weight percent of organic complex and geometrical calculations. The porosity reduction led to improving the optoelectrical properties of metal grid TCs ($R_s < 6 \Omega \text{sq}^{-1}$ at $T_{550\text{nm}} = 91\%$) and preventing serious damage ($\Delta R/R_0 < 6\%$) from the strong IFE between the metal and the substrate during the transfer process. In addition, we verified that the porosity reduction resulted in significantly enhancing an electromechanical durability of the flexible metal grid TCs under static and dynamic bending stresses. The OLED based on flexible metal grid TCs as anode electrodes was demonstrated. The uniformity, reliability and scalability of the metal grid TCs should be further improved by the combination of uniform pressing-stable detaching system and the exact control of fluidic properties (viscosity and surface tension)

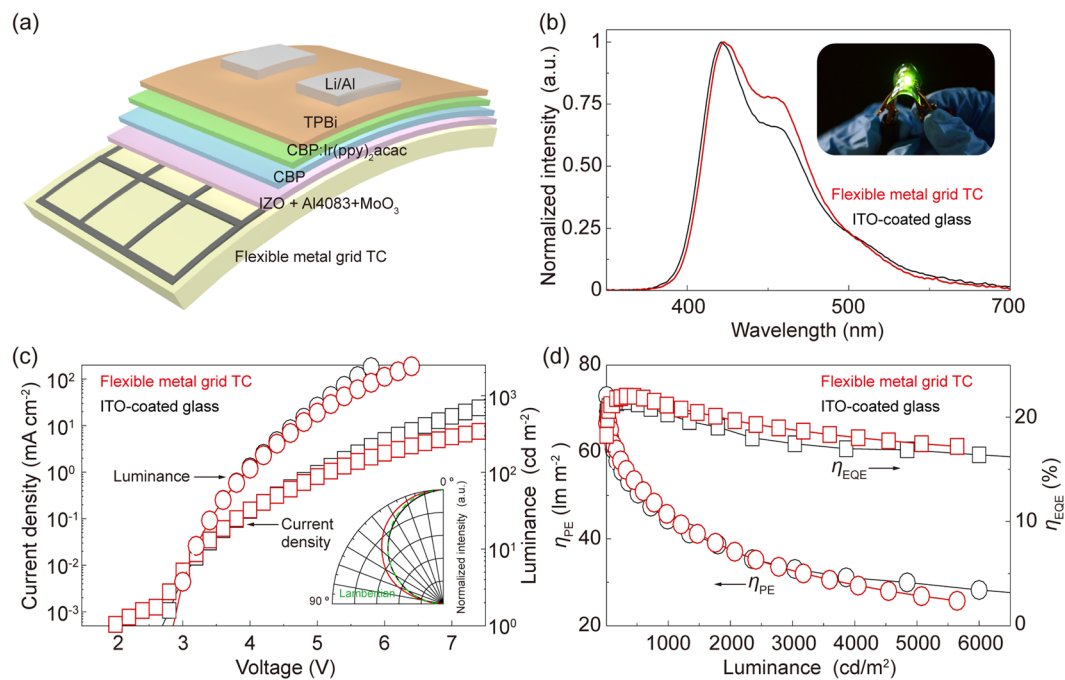


Figure 5. (a) Schematic illustration of the flexible OLEDs prepared using the embedded metal grid TC. (b) The normalized intensity spectra of the flexible OLEDs. The inset shows a photograph of the flexible OLEDs working at high luminance. (c) Current density–voltage characteristics and luminance–voltage characteristics of the proposed flexible OLEDs and reference cells on ITO-coated glass substrates. The inset shows the angular dependences of the normalized intensity. (d) Power efficiency and external quantum efficiency vs luminance.

before this technology can be commercialized. We believe that this strategy can provide a useful approach to enhance optoelectrical properties and an electromechanical durability of solution-processed metallic TCs for the development of next-generation flexible optoelectronic devices.

Methods

Ag ionic ink. The Ag ionic ink (TEC-IJ-060, Inktec) consisted of Ag ions (Ag alkyl carbamate complexes), a base solvent (methanol and toluene) and additives. Prior to the TCDI of Ag ionic ink, methanol was evaporated at 100 °C for 10 min to improve the concentrated ink filling. The Ag alkyl carbamate complexes were decomposed to Ag NPs, carbon dioxide, and the corresponding alkyl amines by heating above 50 °C for a few minutes³⁴.

PDMS mold. The PDMS solution (Sylgard 184, Dow Corning) was generated by mixing the silicon elastomer kit and a curing agent (10:1), and this mixture was poured onto a SU-8 master. After PDMS curing at 100 °C for 1 hour, a PDMS mold was carefully released from the SU-8 master. In the PDMS mold, the grid-patterned cavity was designed with a width (w) of 15 μm and a spacing (s) of 250 μm by calculating the geometrical shadow zone, $T = s^2/(s + w)^2$. The value of a cavity height was limited to 7.5 μm to prevent the destruction of Ag NP structures during the detachment of PDMS mold. However, the value of $T_{550\text{nm}}$ measured from the metal grid TCs was higher than that obtained using the geometrical calculation of grid-patterned mold due to mold deformation (93.2 and 89%, respectively).

Effect of pressure. The effect of P , ranged from 30 to 300 kPa, was examined by considering the Poiseuille's law (h_f^4 is inversely proportional to ΔP)³⁷. At 30 kPa, most of the ink was not captured inside the grid-patterned mold due to a large value of h_f . The ink was effectively captured inside the mold cavity over 100 kPa. The pressure was optimized at 120 kPa by comparing R_s and $T_{550\text{nm}}$ of the metal grid TCs. Also, the relatively uniform P based on horizontal levels led to decreasing both R_s and resistance fluctuations of the metal grids.

Transfer process. All types of glass substrate, including soldalime glass and borosilicate glass, were treated using 1 H, 1 H, 2 H, 2 H-perfluorooctyl-trichlorosilane (448931, Sigma-Aldrich) for 3 min in a vacuum chamber. After the sintering process, a metal grid-patterned glass substrate (soldalime) was re-treated with the fluorinated silane. The NOA 81 solution was poured onto the metal grid-patterned glass substrate, and it was covered by a borosilicate glass substrate. After UV exposure, the borosilicate glass substrate was detached from the NOA film, and then the metal grid-embedded within NOA 81 film (its thickness of 150 μm) was detached from the soldalime glass substrate.

Fabrication of flexible organic light-emitting diodes. The IZO film (~50 nm) was deposited on the flexible metal grid TCs using an RF sputtering system (RF power: 120 W). The PEDOT:PSS (Clevios PVP AI4083,

Heraeus, 45 nm) layers were spin-coated on the top of the IZO films. PEDOT:PSS was coated also on pre-coated ITO glass substrates ($<12 \Omega \text{ sq}^{-1}$, AMG Inc., Korea) as a reference after O_2 plasma treatment (70 W, 1 min). The samples with PEDOT:PSS were dried to remove any residual solvent at 100°C for 10 min on the hot plate. Finally, the PEDOT:PSS-coated samples were loaded into a thermal evaporator for deposition of organic, metal oxide layers, and metal electrodes under high vacuum (3×10^{-6} Torr) conditions. The stacked multilayers of OLEDs were composed of MoO_3 (10 nm)/CBP (20 nm)/CBP doped with 7 wt% of $\text{Ir}(\text{ppy})_2\text{acac}$ (20 nm)/TPBi (55 nm)/LiF (1 nm)/Al (100 nm).

DCB test. The Ag NP film/glass substrate (sodalime) specimens were fabricated with the size of $37.5 \text{ mm} \times 9 \text{ mm}$. The specimens were sandwiched by an additional glass beam using an epoxy (353ND, Epoxy Technology). The final structure of the DCB test specimen was the glass substrate/epoxy/Ag/glass substrate. The connection parts with the DCB test machine and aluminum loading tabs were attached to the specimens with the selective epoxy (DP420, 3M) and the specimens were cured at 120°C for 1 h in a convection oven.

Characterization. The images of the metal grid TCs were measured using field-emission SEM (S-4800, Hitachi). Cross-sectional images of the metal grid TCs were measured using FIB-SEM (Helios Nanolab 600, FEI), and the surface roughness of the flexible metal grid TCs was measured using AFM (XE-100, Park Systems). The transmittance spectra were measured using a UV-VIS-NIR spectrophotometer (Lambda 1050, Perkin-Elmer). The R_s of the metal grid TCs was measured using the two-terminal method and four-point probe method (4200-SCS, Keithley)³⁸. Two electrodes between the metal grids, separated by a square area (25 mm^2), were fabricated using conductive pens (CW2200MTP and CW2900, ITW Chemtronics).

References

1. Ellmer, K. Past achievements and future challenges in the development of optically transparent electrodes. *Nat. Photonics* **6**, 809–817 (2012).
2. Kumar, A. & Zhou, C. The race to replace tin-doped indium oxide: which material will win? *ACS Nano* **4**, 11–14 (2010).
3. Vosgueritchian, M. *et al.* Highly conductive and transparent PEDOT:PSS films with a fluorosurfactant for stretchable and flexible transparent electrodes. *Adv. Funct. Mater.* **22**, 421–428 (2012).
4. Bae, S. *et al.* Roll-to-roll production of 30-inch graphene films for transparent electrodes. *Nat. Nanotechnol.* **5**, 574–578 (2010).
5. Zhang, D. *et al.* Transparent, conductive, and flexible carbon nanotube films and their application in organic light-emitting diodes. *Nano Lett.* **6**, 1880–1886 (2006).
6. Mutiso, R. M. *et al.* Integrating simulations and experiments to predict sheet resistance and optical transmittance in nanowire films for transparent conductors. *ACS Nano* **7**, 7654–7663 (2013).
7. Wu, H. *et al.* A transparent electrode based on a metal nanotrough network. *Nat. Nanotechnol.* **8**, 421–425 (2013).
8. Han, B. *et al.* Uniform self-forming metallic network as a high-performance transparent conductive electrode. *Adv. Mater.* **26**, 873–877 (2014).
9. Bao, C. *et al.* *In situ* fabrication of highly conductive metal nanowire networks with high transmittance from deep-ultraviolet to near-infrared. *ACS Nano* **9**, 2502–2509 (2015).
10. Choi, D. Y. *et al.* Annealing-free, flexible silver nanowire–polymer composite electrodes *via* a continuous two-step spray-coating method. *Nanoscale* **5**, 977–983 (2013).
11. Kang, M.-G. & Guo, L. J. Nanoimprinted semitransparent metal electrodes and their application in organic light-emitting diodes. *Adv. Mater.* **19**, 1391–1396 (2007).
12. Park, J. H. *et al.* Flexible and transparent metallic grid electrodes prepared by evaporative assembly. *ACS Appl. Mater. Inter.* **6**, 12380–12387 (2014).
13. Groep, J. *et al.* Transparent conducting silver nanowire networks. *Nano Lett.* **12**, 3138–3144 (2012).
14. Yu, J.-S. *et al.* Silver front electrode grids for ITO-free all printed polymer solar cells with embedded and raised topographies, prepared by thermal imprint, flexographic and inkjet roll-to-roll processes. *Nanoscale* **4**, 6032–6040 (2012).
15. Yu, J.-S. *et al.* Transparent conductive film with printable embedded patterns for organic solar cells. *Sol. Energy Mater. Sol. Cells* **109**, 142–147 (2013).
16. Li, Y. *et al.* High-efficiency robust perovskite solar cells on ultrathin flexible substrates. *Nat. Commun.* **7**, 10214 (2016).
17. Oh, Y. S. *et al.* Direct imprinting of thermally reduced silver nanoparticles *via* deformation-driven ink injection for high-performance, flexible metal grid embedded transparent conductors. *RSC Adv.* **5**, 64661–64668 (2015).
18. Oh, Y. S. *et al.* High-performance, solution-processed, embedded multiscale metallic transparent conductors. *ACS Appl. Mater. Inter.* **8**, 10937–10945 (2016).
19. Jung, S. *et al.* Extremely flexible transparent conducting electrodes for organic devices. *Adv. Energy Mater.* **4**, 1300474 (2014).
20. Jang, Y. *et al.* Invisible metal-grid transparent electrode prepared by electrohydrodynamic (EHD) jet printing. *J. Phys. D: Appl. Phys.* **46**, 155103 (2013).
21. Schneider, J. *et al.* Electrohydrodynamic nanodrip printing of high aspect ratio metal grid transparent electrodes. *Adv. Funct. Mater.* **26**, 833–840 (2016).
22. Zhang, Z. *et al.* Controlled inkjetting of a conductive pattern of silver nanoparticles based on the coffee-ring effect. *Adv. Mater.* **25**, 6714–6718 (2013).
23. Lee, Y. *et al.* Thermal pressing of a metal-grid transparent electrode into a plastic substrate for flexible electronic devices. *J. Mater. Chem. C* **4**, 7577–7583 (2016).
24. Kim, I. *et al.* Roll-offset printed transparent conducting electrode for organic solar cells. *Thin Solid Films* **580**, 21–28 (2015).
25. Ko, S. H. *et al.* Direct nanoimprinting of metal nanoparticles for nanoscale electronics fabrication. *Nano Lett.* **7**, 1869–1877 (2007).
26. Park, I. *et al.* Nanoscale patterning and electronics on flexible substrate by direct nanoimprinting of metallic nanoparticles. *Adv. Mater.* **20**, 489–496 (2008).
27. Kim, J. H. *et al.* Enhancing adhesion of screen-printed silver nanopaste films. *Adv. Mater. Interfaces* **2**, 1500283 (2015).
28. Lee, I. *et al.* Interfacial toughening of solution processed Ag nanoparticle thin films by organic residuals. *Nanotechnology* **23**, 485704 (2012).
29. Gerard, D. A. & Koss, D. A. Porosity and crack initiation during low cycle fatigue. *Mater. Sci. Eng., A* **129**, 77–85 (1990).
30. Lee, H.-Y. *et al.* Effects of bending fatigue on the electrical resistance in metallic films on flexible substrates. *Met. Mater. Int.* **16**, 947–951 (2010).
31. Sim, G.-D. *et al.* Tensile and fatigue behaviors of printed Ag thin films on flexible substrates. *Appl. Phys. Lett.* **101**, 191907 (2012).
32. Kim, S. *et al.* Tensile characteristics of metal nanoparticle films on flexible polymer substrates for printed electronics applications. *Nanotechnology* **24**, 085701 (2013).

33. Eun, K. *et al.* Electromechanical properties of printed copper ink film using a white flash light annealing process for flexible electronics. *Microelectron. Reliab.* **55**, 838–845 (2015).
34. Kwak, W.-G. *et al.* Preparation of silver-coated cotton fabrics using silver carbamate *via* thermal reduction and their properties. *Carbohydr. Polym.* **115**, 317–324 (2015).
35. Yeo, J. *et al.* Flexible supercapacitor fabrication by room temperature rapid laser processing of roll-to-roll printed metal nanoparticle ink for wearable electronics application. *J. Power Sources* **246**, 562–568 (2014).
36. Choi, D. Y. *et al.* Highly conductive, bendable, embedded ag nanoparticle wire arrays *via* convective self-assembly: Hybridization into ag nanowire transparent conductors. *Adv. Funct. Mater.* **25**, 3888–3898 (2015).
37. Cheng, W. *et al.* Nanopatterning self-assembled nanoparticle superlattices by moulding microdroplets. *Nat. Nanotechnol.* **3**, 682–690 (2008).
38. Hsu, P.-C. *et al.* Performance enhancement of metal nanowire transparent conducting electrodes by mesoscale metal wires. *Nat. Commun.* **4**, 2522 (2013).

Acknowledgements

This work was supported by the KUSTAR-KAIST Institute, and by the Basic Science Research Program (N01160766) of the National Research Foundation of Korea (NRF) funded by the Ministry of Education, and the Global Leading Technology Program (N10042433) funded by the Ministry of Trade, Industry and Energy, and by the Research Program “Technology Development of Low Cost Flexible Lighting Surface”, which is a part of the R&D Program of Electronics and Telecommunications Research Institute (ETRI).

Author Contributions

Y.S.O. conceived the research. I.P. and H.J.S. supervised the research. Y.S.O., D.Y.C., S.U.L., K.S.Y., S.Y. and T.S.K. designed the experiments. Y.S.O., H.S.C., J.L. and H.L. performed the experiments. Y.S.O., H.S.C., J.L., H.L., D.Y.C., S.U.L., K.S.Y., S.Y., T.S.K., I.P. and H.J.S. contributed to the manuscript preparation. All authors have given approval to the final version of the manuscript.

Additional Information

Supplementary information accompanies this paper at doi:[10.1038/s41598-017-11475-8](https://doi.org/10.1038/s41598-017-11475-8)

Competing Interests: The authors declare that they have no competing interests.

Publisher's note: Springer Nature remains neutral with regard to jurisdictional claims in published maps and institutional affiliations.



Open Access This article is licensed under a Creative Commons Attribution 4.0 International License, which permits use, sharing, adaptation, distribution and reproduction in any medium or format, as long as you give appropriate credit to the original author(s) and the source, provide a link to the Creative Commons license, and indicate if changes were made. The images or other third party material in this article are included in the article's Creative Commons license, unless indicated otherwise in a credit line to the material. If material is not included in the article's Creative Commons license and your intended use is not permitted by statutory regulation or exceeds the permitted use, you will need to obtain permission directly from the copyright holder. To view a copy of this license, visit <http://creativecommons.org/licenses/by/4.0/>.

© The Author(s) 2017